Synthesis of Ce 2 O 2 S and Gd 2(1− y) Ce 2 y O 2 S Nanoparticles and Reactivity from in Situ X-ray Absorption Spectroscopy and X-ray Photoelectron Spectroscopy

Clément Larquet, Anh-Minh Nguyen, Mario Ávila-Gutiérrez, Lionel Tinat, Benedikt Lassalle-Kaiser, Jean-Jacques Gallet, Fabrice Bournel, Andrea Gauzzi, Clément Sanchez, Sophie Carenco

HAL Id: hal-01635618
https://hal.sorbonne-universite.fr/hal-01635618

Submitted on 15 Nov 2017

Synthesis of Ce_2O_2S and $Gd_{2(1-y)}Ce_{2y}O_2S$ Nanoparticles and Reactivity from *In situ* X-ray Absorption Spectroscopy and X-ray Photoelectron Spectroscopy

Clément Larquet,[1,2] Anh-Minh Nguyen,[1] Mario Ávila-Gutiérrez,[1] Lionel Tinat,[1] Benedikt Lassalle-Kaiser,[3] Jean-Jacques Gallet,[4,3] Fabrice Bournel,[4,3] Andrea Gauzzi,[2] Clément Sanchez,[1] Sophie Carenco,[1,]*

[1] Sorbonne Universités, UPMC Univ Paris 06, CNRS, Collège de France, Laboratoire de Chimie de la Matière Condensée de Paris, 4 place Jussieu, 75005 Paris, France

[2] Sorbonne Universités, UPMC Univ Paris 06, CNRS, IRD, MNHN, Institut de Minéralogie, de Physique des Matériaux et de Cosmologie, 4, place Jussieu, 75005 Paris, France

[3] Synchrotron SOLEIL, L'Orme des Merisiers, 91192 Saint-Aubin - BP 48, Gif-sur-Yvette Cedex, France.

[4] Sorbonne Universités, UPMC Univ Paris 06, CNRS, Laboratoire de Chimie Physique Matière et Rayonnement, 4 place Jussieu, 75005 Paris, France

*Corresponding author. E-mail: sophie.carenco@upmc.fr

Abstract:

Lanthanide oxysulfide nanoparticles have recently attracted interest in view of potential applications, such as lightening devices and MRI contrast agents, which requires a good stability in air and a controlled surface. In order to address these issues, in this work, air-sensitive Ce_2O_2S nanoparticles of hexagonal shape were successfully prepared and characterized under inert conditions. Bimetallic $Gd_{2(1-y)}Ce_{2y}O_2S$ nanoparticles of similar shape and size were also synthesized for the whole composition range (y from 0 to 1). X-ray diffraction structural data are found to follow Vegard's law up to $y = 0.4$, which is attributed to the loss of stability in air of Ce-rich nanocrystals beyond this threshold. This picture is supported by X-ray absorption spectra taken at the S K- and Ce L_3-edges that show the partial oxidation of sulfide species and of Ce^{III} to Ce^{IV} in the presence of air or water. A complementary near-ambient-pressure X-ray photoelectron spectroscopy study shows that at least two types of oxidized sulfur species form on the nanoparticle surface. Even in Gd_2O_2S nanoparticles that are generally considered to be air-stable, we found that sulfide ions are partially oxidized to sulfate in air. These results unveil the physico-chemical mechanisms responsible for the surface reactivity of lanthanide oxysulfides nanoparticles in air.

Keywords: oxysulfide; cerium; gadolinium; bimetallic nanoparticles; surface reactivity; XANES; S K-edge; NAP-XPS.

1. Introduction

In the last decade, the development of novel methods enabling the synthesis of nanoparticles has resurrected the interest in bianionic materials such as oxysulfides $M_xO_yS_z$. These compounds are particularly attractive as they contains abundant heteroatoms.[1] The combination of lanthanide with oxygen and non-oxidized sulfur has been known for more than sixty years.[2] Since the first report on lanthanide oxysulfides, only few compositions have been synthesized *via* solid state or solid-gas reactions at high temperatures. These synthesis techniques employ various sulfur sources (elemental sulfur, H_2S, or CS_2) as sulfidation agents. Some of them also involve a transition metal, producing bimetallic compounds, such as $Ln_2Ti_2S_2O_5$ and $LnCrOS_2$ (Ln = La-Lu)[3–5], but also $LaInOS_2$ and $La_5In_3S_9O_3$.[6]

Ln_2O_2S nanoparticles have been extensively studied and characterized for their promising magnetic[7–9], photocatalytic[8] and luminescent properties[10,11]. In the latter case, most studied compounds are La_2O_2S,[12–15] Gd_2O_2S[16–21] and Y_2O_2S,[22–30], especially with rare-earth doping (Eu^{III}, Tb^{III}, Yb^{III}, etc.). Doped lanthanide oxysulfides $Ln_2O_2S:Ln^{III}$ nanoparticles (with mostly Ln = La, Gd, Y in the Ln_2O_2S phase) are particularly interesting as luminescent materials in biological media because the oxysulfide phase is an efficient matrix enabling the fluorescence of the doping ion. One important research direction aims at the development of efficient luminescent materials characterized by a long lifetime, which would open the field of *in vivo* imaging.

The synthesis of oxysulfide nanoparticles is challenging, as rare-earth metals have a better affinity with O^{2-} than S^{2-} according to the Hard and Soft Acid and Bases (HSAB) theory. Moreover, the fairly high temperatures required for the formation of the crystalline phase can cause the sintering of the nanoparticles. As a matter of fact, well crystallized Ln_2O_2S nanoparticles have been hitherto obtained only for Ln = La, Pr, Nd, Sm, Eu, Gd, Tb and Y. Ding and coworkers[14] proposed an efficient and versatile synthesis of lanthanide oxysulfide

nanoparticles by thermal decomposition of molecular species in solution, yielding Na-doped Ln_2O_2S (Ln = La, Pr, Nd, Sm, Eu, Gd, Tb). In organic solvents, they obtained small and monodisperse oxysulfide nanoplates of diameters in the 10-25 nm range depending on the lanthanide. Moreover, Pasberg et $al.$ reported Ln_2O_2S nanoparticles containing Lu and Gd.[31]

In this context, cerium oxysulfide Ce_2O_2S nanoparticles would display ideal optical properties owing to the much smaller band-gap energy (brown material) than other Ln_2O_2S compounds, where the band-gap is larger than 3.5 eV for all other Ln. Such a low band-gap permits an absorption in the visible-light range, which is desirable for application in photocatalysis. Moreover, the two possible oxidation states of cerium (Ce^{III} and Ce^{IV}) would make Ce_2O_2S a promising material for catalytic or electrocatalytic reactions. The most suitable material for these applications would be nanoparticles of Ce_2O_2S, in order to get a high surface to volume ratio and to benefit from the numerous available processes to design catalysts with nanoparticles.

To the best of our knowledge, the synthesis of colloidal cerium oxysulfide nanoparticles including Ce_2O_2S was not reported yet, despite the fact that the bulk phase is known since the 1950's.[2,32] One difficulty is that the oxidation state of cerium can be either Ce^{III} (the oxidation state in Ce_2O_2S) or Ce^{IV}. As a result, the oxidation of bulk Ce_2O_2S led to mixed-valence crystalline bulk phases, such as $Ce_2O_{2.5}S$,[32–34] $Ce_4O_4S_3$[35] or $Ce_6O_6S_4$.[36] Systems including nanoscaled Ce_2O_2S supported on graphitized carbon[37] or N and S-doped carbon[38] were recently developed for applications in Li-ion batteries and ORR reaction respectively.

Here, we report on the first synthesis of Ce_2O_2S nanoparticles and on their characterization by transmission electron microscopy (TEM) and x-ray diffraction (XRD). We show that their structure evolves rapidly in air, but also in the presence of water. In $situ$ X-ray absorption spectroscopy evidences the partial oxidation of Ce^{III} into Ce^{IV} and the formation of oxidized

sulfur species. The latter were also found on the surface of Gd_2O_2S nanoparticles, although these nanoparticles are generally considered stable in air. Bimetallic $Gd_{2(1-y)}Ce_{2y}O_2S$ nanoparticles of similar shape and size with y ranging from 1 to 90 % are also synthesized. The lattice parameter a was measured and compared to the theoretical value obtained from Vegard's law. We identified three regimes, related to the stability of the nanoparticles in air. Above 40 % of cerium, the nanoparticles were not air-stable. Nevertheless, the nanoparticles of $Gd_{2(1-y)}Ce_{2y}O_2S$ keep the Ln_2O_2S structure and morphology up to 80 %, making gadolinium an efficient co-cation to protect the cerium oxysulfide structure. Thus, cerium-rich nanoparticles could be used even in ambient air unlike Ce_2O_2S nanoparticles whose high sensitivity to air would cause the material degradation. Lastly, the reactivity of $GdCeO_2S$ ($y = 50$ %) and Gd_2O_2S in water vapor and O_2 was investigated using near-ambient-pressure X-ray photoelectron spectroscopy. This study confirmed the swift and partial oxidation of Ce^{III} to Ce^{IV}. We showed that not only sulfate, but also S^{IV} species form on the nanoparticles surface, which was attributed to intermediate sulfite ions. To the best of our knowledge, this study constitutes the first report on Ce_2O_2S nanoparticles, the first example of bimetallic lanthanide oxysulfide phase with large solubility, and an unprecedented investigation of the surface reactivity of metal oxysulfides.

2. Results and discussion

2.1. Synthesis of Ce_2O_2S nanocrystals

$Ce(acac)_3$ hydrate was reacted at 310 °C for 30 min with a stoichiometric amount of sulfur (0.5 equiv. *vs.* Ce) in a mixture of oleylamine, oleic acid and 1-octadecene, in the presence of Na(oleate) hydrate (see experimental section). The reaction was performed under inert atmosphere. In a first attempt, the particles were isolated and washed under ambient air. The product was dark brown at first but turned greenish after a few hours and light brown after a

few weeks (Figure S1), suggesting product decomposition in air. Consistent with this observation, the X-ray diffraction pattern matched the pattern of Ce_2O_2S a few hours after the synthesis and evolved into another pattern similar to that of CeO_2 in a time span of two weeks (Figure S2). A similar observation was previously reported in bulk samples as well but in a time span of months[32] and the final product was identified by Sourisseau et al[33,34] to be $Ce_2O_{2.5}S$ with an insertion of oxygen in the layer of cerium oxide owing to a partial oxidation of Ce^{III} in Ce^{IV}. This suggests that washing and handling of the nanoparticles in air was inappropriate, although the synthetic route itself was efficient.

To overcome this issue, we isolated the nanoparticles from the crude product and washed them with anhydrous solvents in the inert atmosphere of a glovebox ($H_2O < 0.5$ ppm, $O_2 < 0.5$ ppm). Transmission Electron Microscopy (TEM) carried out on these nanoparticles confirmed the formation of nanoplates whose dimensions vary between 10 to 20 nm in length and 1.5 to 2.5 nm in thickness (Figure 1A). Because of the high amount of remaining ligands on the nanoparticles (washing them in the glovebox is a hard process), we were not able to perform High Resolution Transmission Electron Microscopy (HRTEM).

Despite their small size, X-ray diffraction pattern (XRD) confirmed the crystalline structure of Ce_2O_2S nanoparticles (Figure S3). The pattern matches the reference pattern of hexagonal Ce_2O_2S. Diffraction peaks have different width, which is related to the anisotropy of the nanoparticles shape. Scherrer's formula applied to the (110) diffraction peak gives an average crystal domain size in the range of 8-14 nm, consistent with the observed width of the nanoplates. Hence, each nanoplate is made of a single nanocrystal. Selected-area electronic diffraction (SAED) performed on a few nanoparticles confirmed their good crystalline properties, as the *d*-spacings of the diffraction rings (Figure 1B) match well those of the Ce_2O_2S reference structure (JCPDS 26-1085).
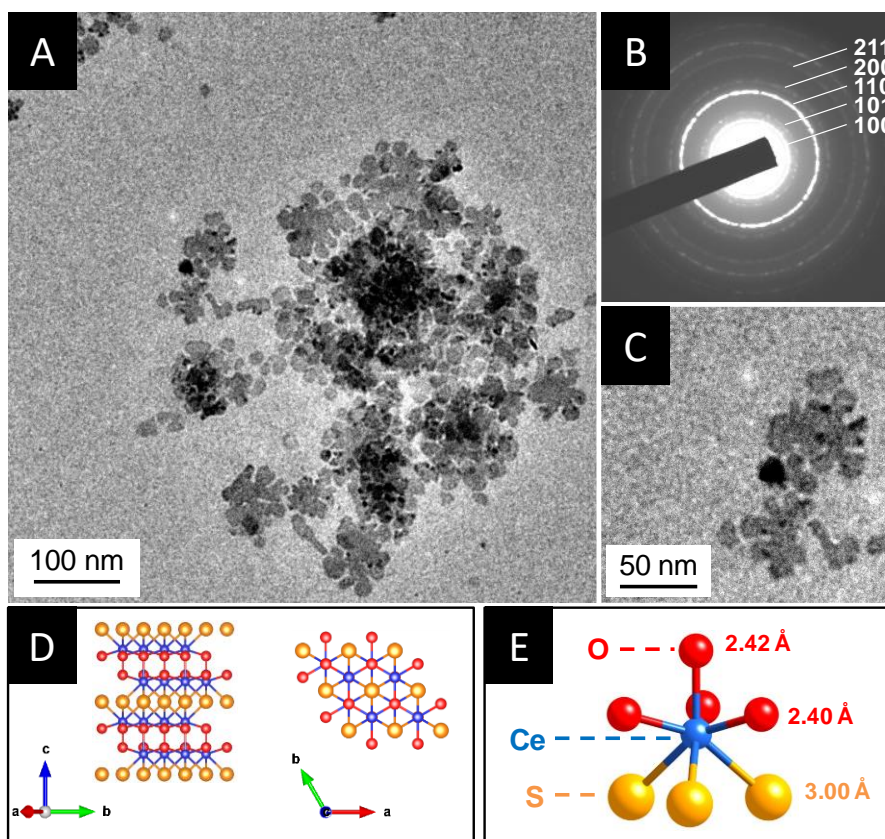
Figure 1: TEM image (A) and the corresponding diffraction pattern (B) of representative Ce_2O_2S nanoparticles. (C) Zoom on the Ce_2O_2S nanoplates. (D) Representation of the lamellar and hexagonal structure of Ce_2O_2S (JCPDS 02-2554) and (E) cerium environment in the structure.

Energy-dispersive X-Ray spectroscopy (EDS) was performed on the nanoparticles. Consistent with the previous work by Ding *et al.*,[14] the data indicate the presence of significant amounts of sodium in the nanoparticles powders. Due to its sensitivity, only a limited washing was performed on the Ce_2O_2S sample. As a result, a high quantity of sodium oleate remained ($Na/Ce \approx 2.7$). According to these authors, the role of sodium is critical on the crystallization of all Ln_2O_2S nanoplates prepared by this route, although recently Lei *et al.* reported on a sodium-free synthesis.[21] The study of the role of this cation on the crystallization process goes beyond the scope of the present work and will be the object of a future paper.

The EDS data indicates a S:Ce ratio of 26 ± 4 %, which illustrates a sulfur deficiency already observed in previous work on other Ln_2O_2S nanoparticles.[14] We thus propose that the Ce_2O_2S nanoplates are terminated by $[Ce_2O_2]^{2+}$ sheets and stabilized by oleate chains.

2.2 Chemical transformation of the nanoparticles exposed to air

As mentioned above, brown-colored Ce_2O_2S becomes green after exposure in air. Isolation and storage of the nanoparticles under controlled inert atmosphere is thus critical. As discussed above, the degradation in air, seen as a loss of the Ln_2O_2S crystalline structure, occurs faster for nanoparticles than for bulk samples, which is attributed to the higher surface to volume ratio of the former. Generally, there is a lack of information regarding the surface reactivity of lanthanide oxysulfide nanoparticles that may be responsible for their degradation. In this work, we employed X-ray Absorption Near Edge Spectroscopy (XANES) at the sulfur K-edge was used to evaluate the sulfur oxidation state in the nanoparticles (Figure 2). Our spectra can be directly compared with those previously obtained on various sulfide, sulfite, sulfonate and sulfate materials which constitute a set of standard spectra.[39–42] From these spectra, one notes that the features of reduced sulfur species are found at low energy while those of oxidized species appear at higher energy. Remarkably, oxidation state of sulfur is often linearly related to the edge energy.[39,43,44]

As reference material, we first measured Gd_2O_2S nanoparticles (*Gd_2O_2S-air*) synthesized following the same route (described in the experimental section). These nanoparticles are stable upon storage in air, during washing steps and storage (see XRD pattern in Figure S4), because Gd only accepts oxidation state (III) under ambient conditions. Second, we prepared Gd_2O_2S nanoparticles, stored and transferred them to the beamline chamber under controlled inert conditions (*Gd_2O_2S-Inert*). The corresponding XANES spectra are presented in Figure 2.

Gd₂O₂S-Inert (Figure 2, green) does not show the broad peak near 2480 eV characteristic of oxidized sulfur (S^{IV} to S^{VI}). On the other hand, this feature is present in the *Gd₂O₂S-air* spectrum (Figure 2, light green). Accordingly, in the 2470-2475 eV region, the peaks corresponding to reduced sulfur are less pronounced, suggesting that the fully reduced sulfur in as-prepared *Gd₂O₂S-Inert* was partially converted into oxidized sulfur upon exposure to air.
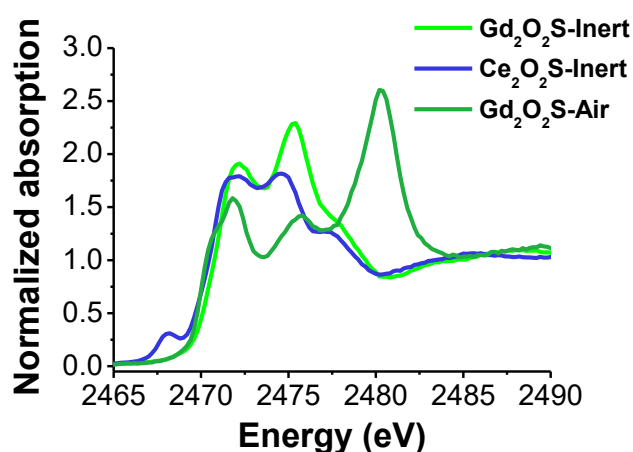

Figure 2: XANES spectra at sulfur K-edge of Gd₂O₂S (*Gd₂O₂S-Inert*) and Ce₂O₂S (*Ce₂O₂S-Inert*) nanoparticles treated and stored under controlled inert atmosphere and Gd₂O₂S (*Gd₂O₂S-air*) treated and stored for five weeks in air.

Since the XANES spectra were collected in fluorescence mode, they reflect both the surface and the core of the samples; sulfur oxides could in principle be either on the surface of the nanoparticles or inside the inorganic core. XRD patterns of both samples are, however, identical, which confirms the crystalline structure of Gd₂O₂S (see XRD pattern in the bottom panel of Figure S4). TEM also confirmed that the size and shape of the nanoparticles is preserved (data not shown). Oxidation of sulfur due to exposure in air is then likely a surface phenomenon. Also, Fourier Transform Infrared spectra exhibit specific peaks corresponding to sulfate functions (Figure S5). To the best of our knowledge, this is the first observation of surface reactivity of Gd₂O₂S, which is usually considered a stable phase in air. *Ce₂O₂S-Inert*

did not show any sign of surface oxidation, as expected from the care taken to avoid air exposure. Its spectrum features an additional contribution at low energy (2468 eV) whose origin is not known at this stage. The small feature at 2468 eV was found to be linked to the presence of cerium and is under investigation.

When the nanoparticles react with air (i.e. with water vapor and/or dioxygen), swift oxidation from Ce^{III} to Ce^{IV} may occur in addition to sulfur oxidation. XANES spectra were then taken at the Ce L_{III}-edge, using an environmental cell in flowing water. The sample was taken out of the glovebox and quickly placed in the cell. Prior to exposure to water, the spectrum presented the characteristic peak of Ce^{III} at 5719.2 eV and two small contributions characteristic of Ce^{IV}, at around 5723 and 5729.5 eV (Figure 3, dark blue spectrum). Due to the brief exposure of the sample to air, the S K-edge spectra presented a small peak in the energy region corresponding to oxidized sulfur (inset of Figure 3, purple spectrum), but most of the sulfur was still reduced, as expected from the *ex situ* spectrum presented above. Following the introduction of water into the cell for a few minutes, the Ce L_{III}-edge spectrum exhibited a strong peak of Ce^{IV} and a small one of Ce^{III} (Figure 3, light blue spectrum). The S K-edge spectrum also exhibits the characteristic features of more oxidized species, namely an intense peak near 2480 eV and minor ones in the 2470-2475 eV range (see Figure 3, light blue spectrum).
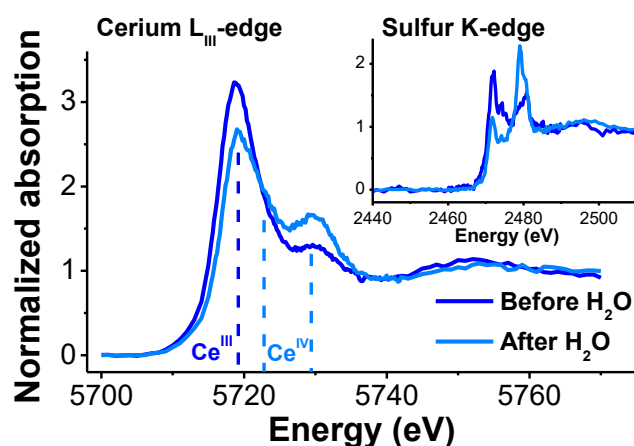

10

Figure 3: *In situ* cerium L_{III}-edge and sulfur K-edge XANES spectra of Ce_2O_2S nanoparticles before and after exposure to water. The position of the peaks attributed to Ce^{III} and Ce^{IV} are consistent with previously published XANES Ce L_{III}-edge spectra.[45,46]

At this stage, we cannot conclude on the different roles of H_2O and of O_2 on the surface oxidation of Gd_2O_2S and on the oxidation of Ce_2O_2S in the core of the nanoparticles, because the water used in the cell contained dissolved O_2. Nevertheless, the *in situ* XANES experiment shows that oxidation is a swift process for the Ce_2O_2S nanoparticles and that both sulfur and cerium are affected.

We presume that the oxidation of sulfur and of cerium may be related to two distinct mechanisms: (i) cerium oxidation leads to the formation of a mixed-valence phase such as $Ce_2O_{2.5}S$; (ii) the oxidation of the sulfides leads to the formation of S^V and of S^{VI} species (eg. sulfates). We argue that the first mechanism is specific to nanoparticles containing cerium while the second one should occur in any Ln_2O_2S phase, including Gd_2O_2S.

Experimentally, we have observed that *Ce_2O_2S-Inert* turns from dark brown to dark green after exposure to air. Dark green is the color of $Ce_2O_{2.5}S$, suggesting a fast oxidation of Ce^{III}. The color of the nanoparticles fades only after several days. Oxysulfate phases[47] were not detected by XRD during ageing under air (Figure S2). At this stage, in the case of Ce_2O_2S, it is unclear whether the oxidized sulfur species are solely at the surface of the nanoparticles or present as amorphous phases. In any case, degradation eventually led to CeO_2 and amorphous species. These amorphous compounds may contain oxidized sulfur, as the XANES experiments (Figure 2 and Figure 3) show the formation of S^V and S^{VI} species when the lanthanide oxysulfide nanoparticles are exposed to air and/or water.

In order to take advantage from the phase stability of Gd_2O_2S and from the potential reactivity of Ce_2O_2S, we attempted the synthesis of Gd-Ce bimetallic oxysulfide nanoparticles,

described by the general formula $Gd_{2(1-y)}Ce_{2y}O_2S$ with y between 0 and 100 %. Cerium loading is defined as $y = n_{Ce} / [n_{Ce} + n_{Gd}]$ where n is the number of moles. To the best of our knowledge, such bicationic nanoparticles of the Ln_2O_2S family without phase separation were never reported before.

2.3 A bridge between Ce_2O_2S and Gd_2O_2S: $Gd_{2(1-y)}Ce_{2y}O_2S$ nanoparticles

Different strategies may be used to obtain bimetallic nanoparticles. Most of the synthetic routes hitherto reported consist of the reaction between small amounts (usually ≤ 1 %) of a dopant and the lanthanide.[12–21,23,25–29,48–54] This approach is justified by the very similar ionic radii of the lanthanides ranging from $r_{La(III)} = 1.03$ Å to $r_{Lu(III)} = 0.86$ Å which favors the formation of a crystalline phase with randomly distributed ions.

Synthesis and composition of the compounds

Following the above considerations, in the present case we simply mixed the precursors of Gd and Ce in appropriate stoichiometry since the radii of Gd and Ce were close enough ($r_{Gd(III)} = 0.94$ Å; $r_{Ce(III)} = 1.01$ Å). This straightforward route enabled us to obtain bimetallic powders in a wide range of composition from $y = 0$ % to $y = 90$ %. In the nanoparticles, the Gd/Ce ratio measured by energy dispersive X-ray spectroscopy (EDS) was found to be consistent with the nominal composition (Figure S6 and Table S1).

From $y = 0$ % to $y = 80$ %, the color of these nanoparticles samples does not change over time. For $y = 90$ %, the powder was initially deep brown, but became light brown within two weeks in air at room temperature, suggesting a decomposition of the structure.

Structural analysis of compounds exposed to air

XRD patterns of nanoparticles isolated in air were systematically performed (Figure S4). For 90 % of cerium, the pattern was not consistent with the reference pattern of Ln_2O_2S, in agreement with the observation mentioned above. XRD pattern shows diffraction peaks of CeO_2 in addition to Ln_2O_2S, as observed for Ce_2O_2S nanoparticles (Figure S8). Below 90 %, the patterns were consistent with Ln_2O_2S but a small shift of the peaks is observed.
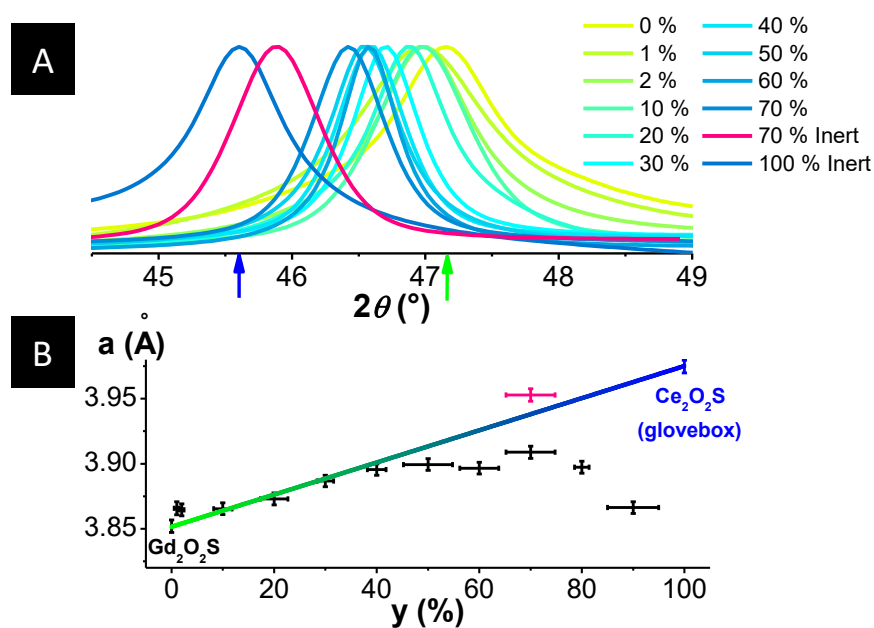

Figure 4: (A) X-ray diffraction normalized (110) peaks fitted using pseudo-Voigt functions for $Gd_{2(1-y)}Ce_{2y}O_2S$ nanoparticles isolated in air and under inert atmosphere for two $Gd_{0.6}Ce_{1.4}O_2S$ and Ce_2O_2S samples (see Figure S9). Vertical arrows indicate the (110) reflection position of Ce_2O_2S (blue, JCPDS 26-1085) and Gd_2O_2S (green, JCPDS 26-1422). (B) Lattice parameter, a as a function of the cerium fraction y. The straight colored line is a linear fit to the data. The data concern bimetallic $Gd_{2(1-y)}Ce_{2y}O_2S$ nanoparticles isolated in air (black dots with error bars) or under inert atmosphere (pink and blue dots with error bars). The lattice parameters of the samples kept under inert atmosphere correspond to the ones expected by the Vegard's law.

The lattice parameter $a = 2 d_{(110)}$ was determined by fitting the position of the (110) and (111) diffraction peaks using pseudo-Voigt curves (Figure 4A). Two regimes are observed. From 0 to 40 %, the lattice parameter follows the Vegard's law expected using the lattice parameters of Gd_2O_2S and Ce_2O_2S (Figure 4B).[55,56] This indicates that both cerium and gadolinium ions partially occupy the same site in the unit cell. From $y > 40$ % to $y = 80$ % the lattice parameter a levels off. To explain this behavior, we envisage the following two scenarios: (i) 40 % is the solubility limit of cerium, or (ii) there is no solubility limit but the phase is not stable in air.

Structural analysis of compound with y $= 70$ % *under inert atmosphere*

In order to clarify the above point, in a complementary experiment, the as-prepared $y = 70$ % compound ($Gd_{0.6}Ce_{1.4}O_2S$) was isolated and washed under inert conditions. The value of the lattice parameter of this sample is larger than that of the sample isolated in air and nicely follows Vegard's law (Figure 4B, pink dot), which supports scenario (ii).

It is interesting to analyze the compounds after air exposure. As discussed above and according to Table S1, the EDS data show that the ratio of lanthanide present in the powder is equal to the nominal ratio. This fact, in addition to the leveling off of the a parameter for $y = 40$ %, suggest that secondary Ce-containing species are formed on the surface of the Ln_2O_2S bimetallic structure as a consequence of air exposure. In order to investigate this question, an additional TEM was carried out.

Transmission electron microscopy on the y $= 0, 37.5, 50$ and 75 % *compounds*

Similar to the case of the Gd_2O_2S and Ce_2O_2S nanoparticles, bimetallic Gd-Ce oxysulfide nanoparticles crystallize in the form of hexagonal nanoplates (Figure 5). Transmission Electron Microscopy images typically display the {001} or {100} facets of the nanoplates. Their width and thickness are 10-20 nm and 2 nm, respectively, somehow larger than the $y=0$

Gd$_2$O$_2$S nanoparticles (7.80 ± 1.28 nm in width and 1.52 ± 0.14 nm in thickness). The width of the nanoparticles are in agreement with Scherrer's crystalline domain size calculated from the (110) reflection peak (Table S2). High-resolution transmission electron microscopy (HRTEM) confirmed that both Gd$_2$O$_2$S and bimetallic nanoparticles are single crystals of Gd$_{2(1-y)}$Ce$_{2y}$O$_2$S. The analysis of the Fourier transforms of the HRTEM images (Figure S10) agrees with the crystal system and with the lattice parameters obtained by means of XRD.

For $y > 70\,\%$, we find some smaller and shapeless nanoparticles that may consist of cerium-containing species that nucleate in the solution during the synthesis or of degraded Gd-Ce oxysulfide nanoparticles exposed to air, as indicated by the smaller a lattice parameter, of these particles.
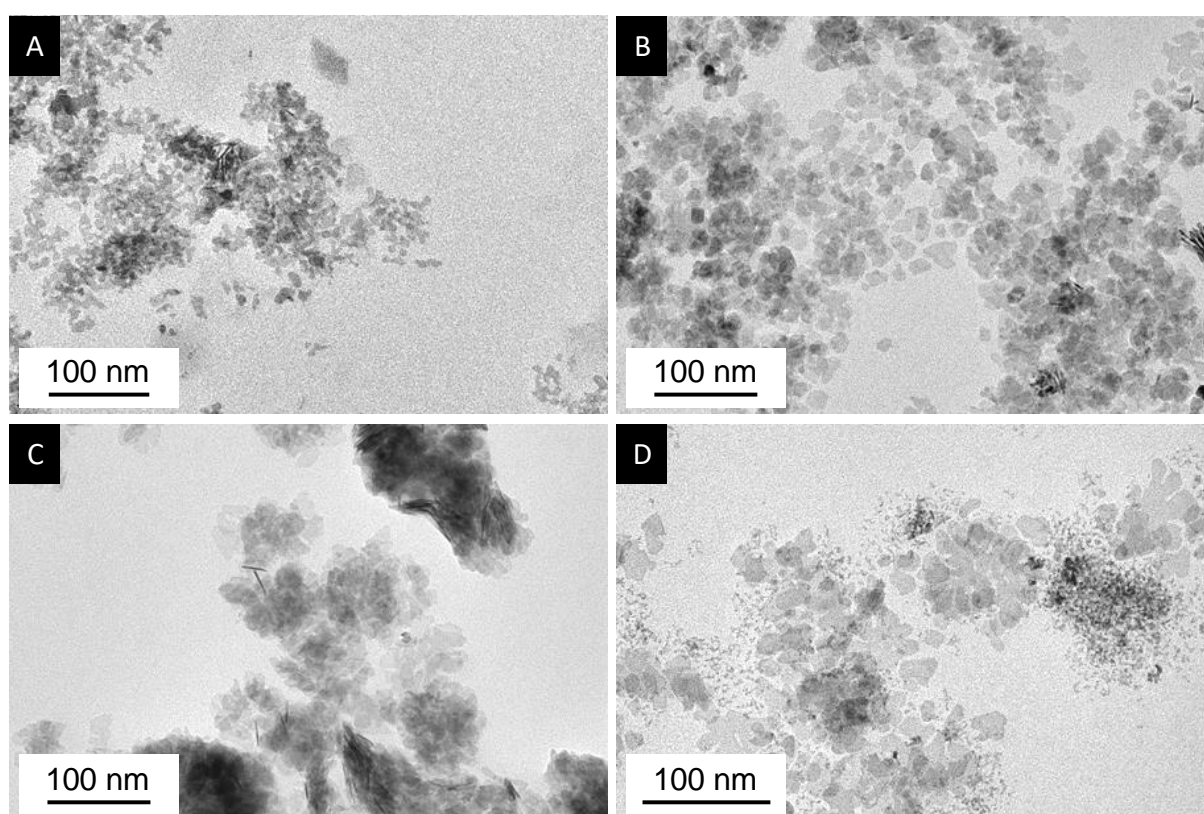

Figure 5: TEM micrographs of Gd$_{2(1-y)}$Ce$_{2y}$O$_2$S nanoparticles containing the following cerium fractions: (A) $y = 0\,\%$, (B) 37.5 %, (C) 50 % and (D) 75 %.

Altogether, the substitution of Gd by Ce in Gd_2O_2S slightly affects the oxysulfide nanoparticles morphology, and nanoplates of dimension 30 nm or smaller are obtained. For $y < 80\ \%$, the reactivity of cerium in $Gd_{2(1-y)}Ce_{2y}O_2S$ is found to be lower than in pure Ce_2O_2S nanoparticles but it is still sufficient to destabilize the structure for $y > 40\ \%$.

2.3 Reactivity toward O_2 and H_2O: comparison between Gd_2O_2S and $GdCeO_2S$

So far, we have discussed the effect of air as an oxidizing medium, without differentiating the roles of water and of dioxygen. In order to address this question, a Near-Ambient-Pressure X-Ray Photoelectron Spectroscopy (NAP-XPS) facility of the UPMC installed at the TEMPO beamline of SOLEIL was used as a surface analysis technique. We considered the following two scenarios for the oxidation of sulfur and of cerium: (i) the oxidation of both elements occurs independently; (ii) one of the two ions (Ce^{III} and S^{-II}) delays the oxidation of the other ion. In case (i), sulfur in $GdCeO_2S$ and in Gd_2O_2S should oxidize at the same rate. In case (ii), the sequential oxidation of cerium and of sulfur, or vice-versa, should be observed by XPS. In order to verify these two scenarios, fresh Gd_2O_2S and $GdCeO_2S$ ($y = 50\ \%$) nanoparticles were synthesized, isolated in air, and drop-casted on gold-covered silicon wafer. Exposure to air was limited and the samples were stored under inert atmosphere and introduced in the set-up via a glove bag connected to the load lock of the NAP-XPS.

The nanoparticles were analyzed at room temperature under vacuum, and then under water pressure, a mixture of water and oxygen, and back under vacuum. The two samples were deposited on a single sample-holder and subsequently exposed to exactly the same atmospheres. Thoroughly degassed water vapor was introduced before introducing the O_2 gas, for the former gas is less oxidizing than the latter. O_2 was then introduced along with water, because obtaining ultra-high-vacuum conditions after having introduced water would require baking the vacuum chamber for a long time not compatible with the constraints set by

synchrotron runs. For the same reason, the last measurements under vacuum conditions were actually carried out under a residual background pressure of water.

Binding energies (B.E.) were calibrated using the Au 4f doublet, as described in Table S3. S 2p and Gd 4d photoemission spectra were collected in a single sweep in the 135-175 eV region of B.E. (Figure 6). The Ce $3d_{3/2}$ and Ce $3d_{5/2}$ B.E. were also monitored in the 870-920 eV region for the $GdCeO_2S$ nanoparticles (Figure 7A). As shown in Figure 7C, we successfully determined the Ce^{III} fraction by using a careful fitting procedure of the intensity which takes into account the overlap of the spin-orbit split peak (Figure 7B).
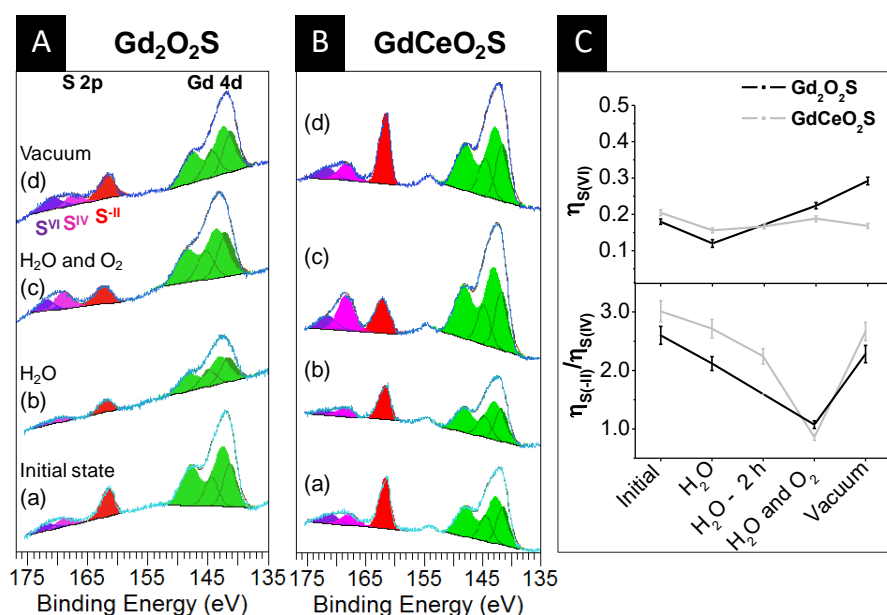

Figure 6: room temperature NAP-XPS spectra of air-exposed samples of (A) Gd_2O_2S and (B) $GdCeO_2S$ nanoparticles collected using an incident photon energy of 735 eV at the following conditions: (a) ultra-high vacuum (10^{-9} mbar); (b) H_2O pressure of 0.2 mbar; (c) Mixture of H_2O (0.2 mbar) and O_2 (0.2 mbar) partial pressures; (d) Vacuum obtained upon pumping down the chamber after (c). (B) For $GdCeO_2S$, an additional spectrum was also collected after exposing the sample to water vapor for two hours without beam to avoid radiation damage. Color code: S 2p doublet in red (S^{-II}), pink (S^{IV}) and purple (S^{VI}); Gd 4d doublets in light green and deep green (shake-down satellite peaks).[57] The fitting curves (in brown) are mostly

superimposed with the experimental curves. (C) Top: S^{VI} fraction ($\eta_{S(VI)}$); Bottom: S^{-II}/S^{IV}

fraction ratio ($\eta_{S(-II)} / \eta_{S(IV)}$). See Table S3 for the details of the fitting procedure.

In all spectra, the sulfide species are identified by a S $2p_{3/2}$ doublet at 161.6 ± 0.3 eV (Figure

6A).[58] Oxidized sulfur is also always present and confirms the XANES result that samples

whose work-up was carried out under air are already partially oxidized. Here, oxidized sulfur

is composed of two major oxidation species that we identify as S^{IV} and S^{VI}. Each S $2p_{3/2}$

spectrum was fitted by a double peak; the B.E. of the lower-energy component was

168.1 ± 0.7 eV for S^{IV} (in pink) and 171.3 ± 0.5 eV for S^{VI} (in purple). The relative area of

each contribution allowed us to plot the ratios of the species for different atmospheres (Figure

6C). For both nanoparticles samples, the Gd spectrum showed no significant evolution, as

expected. The exposure of both Gd_2O_2S and $GdCeO_2S$ samples to water vapor led to a partial

S^{-II} - S^{IV} conversion within 2 hours (Figure 6C); the S^{-II} species correspond to the oxysulfide,

while S^{IV} is attributed to sulfites ions $(SO_3)^{2-}$ forming an step during the sulfide to sulfate

transformation.[59] The addition of O_2 in the chamber led to an increase of S^{IV} concentration

within a few minutes, suggesting that O_2 is a stronger oxidizing agent than water.

The evolution of the S^{VI} fraction is more complex. Initially, the S^{VI} species are attributed to

sulfates formed during the short exposure of the nanoparticles to air. For both samples, this

fraction does not significantly decrease during subsequent treatments, suggesting that the S^{VI}

formed in the room atmosphere prior to the XPS measurement is irreversible. In Gd_2O_2S, the

quantity of S^{VI} species increases during the last steps of exposure to O_2 and of pumping.

However, in $GdCeO_2S$, this quantity remains almost constant over the course of the further

treatments (Figure 6C). It is possible that Ce^{III} was playing a sacrificial role, thus preventing

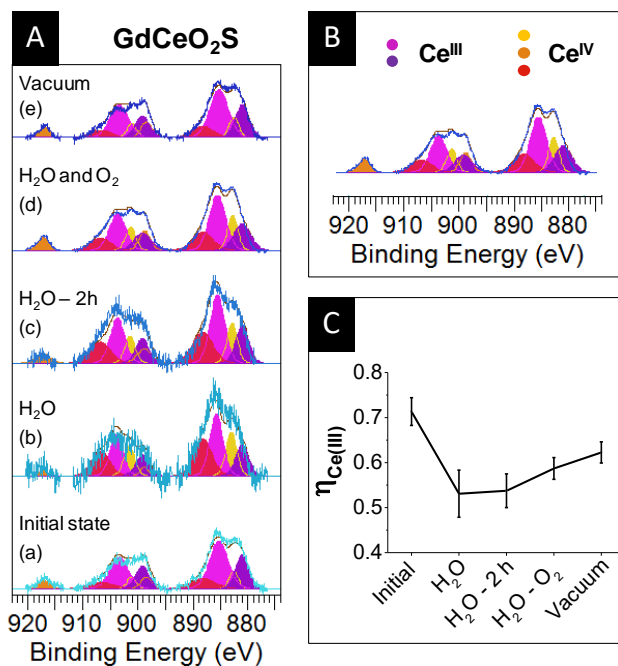sulfur from further oxidation (Figure **7**).

Figure 7: (A) Ce 3d NAP-XPS spectra of GdCeO$_2$S nanoparticles measured with an incident photon energy of 1100 eV and after background subtraction. The Ce^{III} species are represented by the pink and violet peaks. Yellow, orange and red peaks are specific to Ce^{IV} species. (a) Ultra-high vacuum (10^{-9} mbar); (b) H$_2$O partial pressure of 0.2 mbar; (c) after two hours of exposure to a H$_2$O partial pressure of 0.2 mbar; (d) H$_2$O partial pressure of 0.2 mbar and O$_2$ partial pressure of 0.2 mbar; (e) Back to vacuum. (B) Typical deconvolution of the Ce^{III} and Ce^{IV} peaks. (C) Evolution of the fraction of Ce^{III} ($\eta_{Ce(III)}$) during the NAP-XPS experiment. See Table S3 for the details of the fitting procedure.

During exposure to water vapor and then to O$_2$, sulfur oxidation is accompanied by an oxidation of Ce^{III} into Ce^{IV} especially during the early stage of exposure to air (Figure 7C). However, this oxidation is limited and the Ce^{III}/Ce^{IV} ratio remains significant, consistent with the fact that the bulk crystal structure, which contains Ce^{III}, is preserved, as observed *ex situ* in the $y = 50$ % samples.

Restoring the high vacuum conditions almost restored the initial S^{-II} fraction and affected the Ce^{III} fraction. Flahaut et al. previously observed a similar reversibility by heating bulk Ce$_2$O$_2$S

up to 1300 °C under vacuum.[32] Ikeue et al. also reported that oxysulfate sheets can be reduced to oxysulfide ones in H_2S atmosphere.[47] Here, the process occurs at room temperature but the ultra-high vacuum conditions play a reducing role; furthermore, the effect is enhanced in nanoparticles owing to the high surface/volume ratio. Having said this, the reversibility of the reduction under vacuum conditions is different from the oxysulfide/oxysulfate transition, since the XRD patterns of our samples did not show any structural modification even after several months. This further supports the argument that the oxido-reduction process is favored at the surface of the nanoparticles.

3. Conclusion

In this article we showed that cerium oxysulfide Ce_2O_2S nanoparticles can be successfully prepared using colloidal synthesis and that these particles are chemically stable under inert atmosphere. Their brown color is identical to that of previously reported bulk samples and the present XANES study shows that they are free of oxidized sulfur species.

We investigated the surface reactivity of related Gd_2O_2S nanoparticles, whose metal cation cannot undergo redox reaction in air. We showed that the formation of oxidized sulfur in air is a swift process, contrary to previous reports on the stability of these nanoparticles in air.

The synthesis of bimetallic $Gd_{2(1-y)}Ce_{2y}O_2S$ nanoparticles was achieved using the same colloidal route. For all y, we find a linear variation of the lattice parameter a with y according to Vegard's law, thus indicating that confirming the substitution of Gd by Ce in the same site. The exposure of the nanoparticles to air revealed three distinct regimes in terms of structure robustness: (i) for $y = 0$-0.4, no structural change was observed; (ii) for $y = 0.5$-0.8 the excess of cerium with respect to the threshold value of 0.4 is ejected from the nanoplates, forming small nanoparticles aside; (iii) for $y > 0.9$, the nanoparticle structure was not stable in air and evolved into CeO_2, as indicated by a *in situ* XANES study showing oxidation of Ce^{III} to Ce^{IV}.
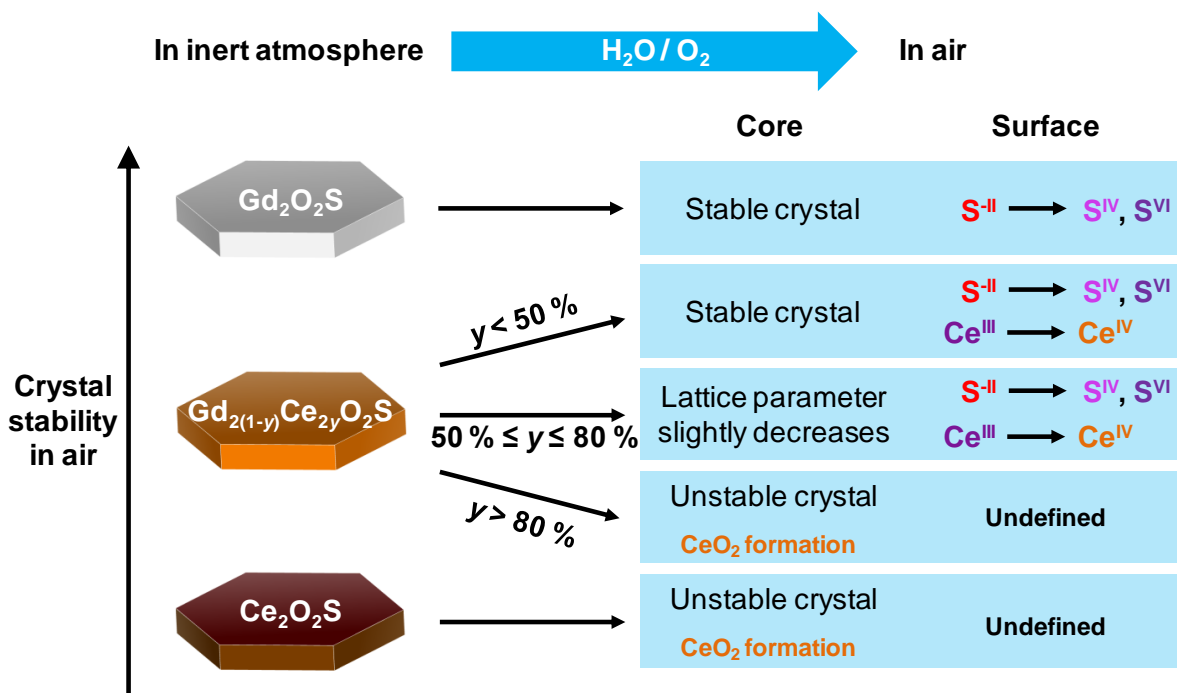
Figure 8: Reactivity of the $Gd_{2(1-y)}Ce_{2y}O_2S$ nanoparticles towards air.

A complementary NAP-XPS study provided deeper insights as to the reactivity of the nanoparticles with air. We found that water vapor favored the formation of intermediate S^{IV} species, proposed to be sulfite anions and that this process is favored by the addition of O_2. In the case of Ce-containing nanoparticles, the process is accompanied by the partial oxidation of Ce^{III} to Ce^{IV}.

Altogether, the reactivity of cerium in lanthanide oxysulfide was found to be tempered by the presence of gadolinium in the same lattice. Optical and magnetic properties of this series of bimetallic nanoscaled oxysulfides will be described in forthcoming article. Generally, the substitution strategy seems to be a promising way to reach new families of nanoscaled metal oxysulfides with tailored physical and chemical properties. The surface reactivity of these objects should be taken into account for applications that require long-term air-stability (e.g. lightening), colloidal stability (e.g. inks), or controlled interaction with living organisms (e.g. MRI contrast agents).

Experimental section

Synthesis of Gd$_{2(1-y)}$Ce$_{2y}$O$_2$S nanoparticles

Bimetallic oxysulfides were prepared *via* a solvothermal reaction including a mixture of organic solvents and metallic complexes. Oleylamine (OM; technical grade, 70 %), oleic acid (OA; technical grade, 90 %), sulfur (S$_8$; ≥ 99.5 %) and sodium oleate (Na(oleate); ≥ 99 %) were purchased from Sigma-Aldrich. 1-octadecene (ODE; technical grade, 90 %) was purchased from Acros Organics. Gadolinium acetylacetonate hydrate (Gd(acac)$_3$·xH$_2$O; 99.9 %) and cerium acetylacetonate hydrate (Ce(acac)$_3$·xH$_2$O; 99.9 %) were purchased from Strem Chemicals. All products were used as received without further purification.

In a typical synthesis of Ce$_2$O$_2$S, Ce(acac)$_3$·xH$_2$O (0.50 mmol), S$_8$ (0.032 mmol), Na(oleate) (0.50 mmol), OM (17 mmol), OA (2.5 mmol) and ODE (32.5 mmol) were added in a 100 mL three-neck flask at room temperature. The brown solution is heated to 120 °C under vacuum for 20 minutes to remove water and other impurities with low boiling points. The mixture is then heated to 310 °C and allowed to stir at this temperature for 30 minutes under purified N$_2$. Then it is left to cool down under N$_2$ to room temperature and is directly transferred to an inert glovebox (H$_2$O: ≤ 0.5 ppm, O$_2$: ≤ 0.5 ppm). The crude product can be dispersed into anhydrous THF. After several centrifugations in anhydrous THF, a brown paste of Ce$_2$O$_2$S nanoparticles is obtained.

In a typical synthesis of GdCeO$_2$S, Gd(acac)$_3$·xH$_2$O (0.25 mmol), Ce(acac)$_3$·xH$_2$O (0.25 mmol), S$_8$ (0.032 mmol), Na(oleate) (0.50 mmol), OM (17 mmol), OA (2.5 mmol) and ODE (32.5 mmol) were added in a 100 mL three-neck flask at room temperature. The brown solution is heated to 120 °C under vacuum for 20 minutes to remove water and other impurities with low boiling points. The mixture is then heated to 310 °C and allowed to stir at this temperature for 30 minutes under purified N$_2$. The transparent solution gradually becomes turbid starting from 280 °C. Then the mixture is left to cool down to room temperature under

N_2. The nanoparticles are isolated using ethanol and washed at least three times using a THF/ethanol (1:5) mixture to remove remaining reagents and organic matter. 40 to 90 mg of dried $Gd_{2(1-y)}Ce_{2y}O_2S$ particles are thus obtained depending on the initial cerium loading.

It should be noted that a significant decrease of the reaction yield (measured after several washing of the nanoparticles in air) is observed along with the amount of cerium introduced in the nanoparticles: starting from 0.5 mmol of lanthanide precursor, a yield of around 100 % *vs.* Gd (95 mg of powder) was obtained for $y = 0$ % (Gd_2O_2S) while a yield of 48 % (45 mg) was obtained for $y = 70$ % ($Gd_{0.6}Ce_{1.4}O_2S$).

X-ray diffraction on powder

The different X-ray diffraction patterns of dry powders were measured on a Bruker D8 diffractometer using Cu Kα radiation at 1.5406 Å. Typical diffractograms were collected with steps of 0.05 ° and a scanning speed of 5 s/point. The backgrounds of the patterns are subtracted using the EVA software. When low noise Si monocristals sample holders were used, the angular position 2θ was corrected by adjusting the sample height (correction around 0.5 to 1 mm, see Figure S7).

Transmission Electron Microscopy and High Resolution TEM

A drop of a diluted solution of $Gd_{2(1-y)}Ce_{2y}O_2S$ dispersed in pure THF was allowed to dry on an amorphous carbon coated copper grid. TEM images were collected with a TWIN 120 (TECNAI SPIRIT) at 120 kV and with a JEOL 100CF. HRTEM was performed on a FEG-TEM JEOL 2100F at 200 kV. For Ce_2O_2S, a drop of a diluted dispersion of the crude nanoparticles in THF was deposited on a copper grid inside the glovebox. The grid was stored under argon swiftly inserted into the transmission electron microscope.

Energy Dispersive X-ray spectroscopy

A small amount of powder was deposited on a carbon adhesive tape on a Scanning Electron Microscope sample holder. EDX analyses were performed on a SEM HITACHI S-3400N at

10 kV. Titanium was chosen as reference and analyses were performed on at least three different zones on the sample.

Near Ambient Pressure X-ray Photoelectron Spectroscopy

X-ray photoelectron spectroscopy was performed on the TEMPO B beamline at SOLEIL on the NAP-XPS set up of UPMC. Samples were deposited from a 30 mg.mL^{-1} solution of dispersed nanoparticles in pure THF onto gold coated (100 nm layer) silica wafers by dip-coating. Spectra were measured under vacuum (10^{-9} mbar), under 0.2 mbar H_2O pressure or under 0.4 mbar H_2O and O_2 pressure (0.2 mbar each). In order to mitigate beam damage, measurements were performed on several spots on the sample surface.

X-ray Absorption Near-Edge Spectroscopy

Sulfur K-edge and cerium L-edge XANES data were collected on the LUCIA beamline at SOLEIL at an electron energy of 2.7 GeV and an average ring current of 450 mA. The incoming photons were selected with a Si (111) double crystal monochromator. 2 to 3 mg of the sample was diluted in *ca* 40 mg of graphite and was compressed to form a 6 mm diameter pellet. Up to seven pellets were fixed with carbon adhesive tape on a copper plate placed in a sample holder inside the measurement chamber. During typical analyses, the pressure in the chamber was maintained around 10^{-2} mbar. Measurements were performed in fluorescence mode using a Bruker silicon drift detector, with an outgoing photon angle of 10 °. All data were normalized to the edge jump and calibrated to the maximum of the first peak of sodium thiosulfate (2470.8 eV).

Fourier Transform Infra-Red spectroscopy

Infrared spectra were collected on a Spectrum 400 (PERKINELMER) spectrometer. The dry sample (1 to 3 mg) was deposited on the attenuated total reflectance (ATR) crystal. Transmittance was measured between 4000 cm^{-1} and 550 cm^{-1} with steps of 0.5 cm^{-1}.

Acknowledgements

References

(1)   Boyd, D. A. Sulfur and Its Role In Modern Materials Science. *Angew. Chemie Int. Ed.* **2016**, 2–19.

(2)   Zachariasen, W. H. Crystal Chemical Studies of the 5f-Series of Elements. VII. The Crystal Structure of Ce2O2S, La2O2S and Pu2O2S. *Acta Crystallogr.* **1949**, *2* (1), 60–62.

(3)   Vovan, T.; Dugué, J.; Guittard, M. Oxysulfures Mixtes de Chrome III et de Terres Rares. *Mater. Res. Bull.* **1978**, *13*, 1163–1166.

(4)   Dugué, J.; Vovan, T.; Villers, J. Etude Structurale Des Oxysulfures de Chrome(Ill) et de Terres Rares. I. Structure de I'Oxysulfure LaCrOS 2. *Acta Crystallogr.* **1980**, *B36*, 1291–1294.

(5)   Dugué, J.; Vovan, T.; Villers, J. Etude Structurale Des Oxysulfures de Chrome(III) et de Terres Rares. II. Structure de I'Oxysulfure CeCrOS2. *Acta Crystallogr.* **1980**, *B36*, 1294–1297.

(6)   Kabbour, H.; Cario, L.; Moëlo, Y.; Meerschaut, A. Synthesis, X-Ray and Optical Characterizations of Two New Oxysulfides: LaInS2O and La5In3S9O3. *J. Solid State Chem.* **2004**, *177* (4–5), 1053–1059.

(7)   Quezel, G.; Ballestracci, R.; Rossat-Mignod, J. Proprietes Magnetiques Des Oxysulfures de Terres Rares. *J. Phys. Chem. Solids* **1970**, *31* (4), 669–684.

(8)   He, W.; Osmulski, M. E.; Lin, J.; Koktysh, D. S.; McBride, J. R.; Park, J.-H.; Dickerson, J. H. Remarkable Optical and Magnetic Properties of Ultra-Thin Europium Oxysulfide Nanorods. *J. Mater. Chem.* **2012**, *22* (33), 16728.

(9)   Biondo, V.; Sarvezuk, P. W. C.; Ivashita, F. F.; Silva, K. L.; Paesano, A.; Isnard, O. Geometric Magnetic Frustration in RE2O2S Oxysulfides (RE=Sm, Eu and Gd). *Mater. Res. Bull.* **2014**, *54*, 41–47.

(10)   Zhao, F.; Yuan, M.; Zhang, W.; Gao, S. Monodisperse Lanthanide Oxysulfide Nanocrystals. *J. Am. Chem. Soc.* **2006**, *128* (36), 11758–11759.

(11)   Gai, S.; Li, C.; Yang, P.; Lin, J. Recent Progress in Rare Earth Micro/Nanocrystals: Soft Chemical Synthesis, Luminescent Properties, and Biomedical Applications. *Chem. Rev.* **2014**, *114* (4), 2343–2389.

(12)   Huang, Y.-Z.; Chen, L.; Wu, L.-M. Crystalline Nanowires of Ln2O2S, Ln2O2S2, LnS2 (Ln) La, Nd), and La2O2S:Eu3+. Conversions via the Boron-Sulfur Method That Preserve Shape. *Cryst. Growth Des.* **2008**, *8* (2), 739–743.

(13)   Liu, Z.; Sun, X.; Xu, S.; Lian, J.; Li, X.; Xiu, Z.; Li, Q.; Huo, D.; Li, J. G. Tb3+- and Eu3+-Doped Lanthanum Oxysulfide Nanocrystals. Gelatin-Templated Synthesis and Luminescence Properties? *J. Phys. Chem. C* **2008**, *112* (7), 2353–2358.

(14)   Ding, Y.; Gu, J.; Ke, J.; Zhang, Y. W.; Yan, C. H. Sodium Doping Controlled Synthesis of Monodisperse Lanthanide Oxysulfide Ultrathin Nanoplates Guided by

Density Functional Calculations. *Angew. Chemie - Int. Ed.* **2011**, *50* (51), 12330–12334.

(15)   Hakmeh, N.; Chlique, C.; Merdrignac-Conanec, O.; Fan, B.; Cheviré, F.; Zhang, X.; Fan, X.; Qiao, X. Combustion Synthesis and up-Conversion Luminescence of La2O2S:Er3+,Yb3+ Nanophosphors. *J. Solid State Chem.* **2015**, *226*, 255–261.

(16)   Song, Y.; You, H.; Huang, Y.; Yang, M.; Zheng, Y.; Zhang, L.; Guo, N. Highly Uniform and Monodisperse Gd 2 O 2 S:Ln 3+ (Ln = Eu, Tb) Submicrospheres: Solvothermal Synthesis and Luminescence Properties. *Inorg. Chem.* **2010**, *49* (24), 11499–11504.

(17)   Thirumalai, J.; Chandramohan, R.; Vijayan, T. a. Synthesis, Characterization and Formation Mechanism of Monodispersed Gd2O2S:Eu3+ Nanocrystals. *J. Mater. Sci. Mater. Electron.* **2011**, *22* (8), 936–943.

(18)   Osseni, S. A.; Lechevallier, S.; Verelst, M.; Dujardin, C.; Dexpert-Ghys, J.; Neumeyer, D.; Leclercq, M.; Baaziz, H.; Cussac, D.; Santran, V.; Mauricot, R. New Nanoplatform Based on Gd2O2S:Eu3+ Core: Synthesis, Characterization and Use for in Vitro Bio-Labelling. *J. Mater. Chem.* **2011**, *21* (45), 18365.

(19)   Liu, J.; Luo, H.; Liu, P.; Han, L.; Zheng, X.; Xu, B.; Yu, X. One-Pot Solvothermal Synthesis of Uniform Layer-by-Layer Self-Assembled Ultrathin Hexagonal Gd2O2S Nanoplates and Luminescent Properties from Single Doped Eu3+ and Codoped Er3+, Yb3+. *Dalt. Trans.* **2012**, *41* (45), 13984.

(20)   Hernández-Adame, L.; Méndez-Blas, A.; Ruiz-García, J.; Vega-Acosta, J. R.; Medellín-Rodríguez, F. J.; Palestino, G. Synthesis, Characterization, and Photoluminescence Properties of Gd:Tb Oxysulfide Colloidal Particles. *Chem. Eng. J.* **2014**, *258* (6), 136–145.

(21)   Lei, L.; Zhang, S.; Xia, H.; Tian, Y.; Zhang, J.; Xu, S. Controlled Synthesis of Lanthanide-Doped Gd 2 O 2 S Nanocrystals with Novel Excitation-Dependent Multicolor Emissions. *Nanoscale* **2017**, *9* (17), 5718–5724.

(22)   Hirai, T.; Orikoshi, T. Preparation of Yttrium Oxysulfide Phosphor Nanoparticles with Infrared-to-Green and -Blue Upconversion Emission Using an Emulsion Liquid Membrane System. *J. Colloid Interface Sci.* **2004**, *273* (2), 470–477.

(23)   Xing, M.; Cao, W.; Pang, T.; Ling, X. Synthesis of Monodisperse Spherical Y2O2S:Yb,Ho Upconversion Nanoparticles. *Solid State Commun.* **2009**, *149* (23–24), 911–914.

(24)   Li, W.; Liu, Y.; Ai, P. Synthesis and Luminescence Properties of Red Long-Lasting Phosphor Y2O2S:Eu3+, Mg2+, Ti4+ Nanoparticles. *Mater. Chem. Phys.* **2010**, *119* (1–2), 52–56.

(25)   Fu, Y.; Cao, W.; Peng, Y.; Luo, X.; Xing, M. The Upconversion Luminescence Properties of the Yb3+–Ho3+ System in Nanocrystalline Y2O2S. *J. Mater. Sci.* **2010**, *45* (23), 6556–6561.

(26)   Wang, H.; Xing, M.; Luo, X.; Zhou, X.; Fu, Y.; Jiang, T.; Peng, Y.; Ma, Y.; Duan, X. Upconversion Emission Colour Modulation of Y2O2S: Yb, Er under 1.55µm and 980nm Excitation. *J. Alloys Compd.* **2014**, *587*, 344–348.

(27)   Han, L.; Hu, Y.; Pan, M.; Xie, Y.; Liu, Y.; Li, D.; Dong, X. A New Tactic to Achieve Y 2 O 2 S:Yb 3+ /Er 3+ up-Conversion Luminescent Hollow Nanofibers. *CrystEngComm* **2015**, *17* (12), 2529–2535.

(28)   Lu, X.; Yang, M.; Yang, L.; Ma, Q.; Dong, X.; Tian, J. Y2O2S:Yb3+, Er3+ Nanofibers: Novel Fabrication Technique, Structure and up-Conversion Luminescent Characteristics. *J. Mater. Sci. Mater. Electron.* **2015**, *26* (6), 4078–4084.

(29) Bakhtiari, H.; Ghasemi, M. R.; Hashemizadeh Aghda, A.; Noorkojouri, H.; Sarabadani, P.; Zeeb, M. Effect of Europium Dopant Concentration on Particle Size and Luminescence of Yttrium Oxysulfide Nanoparticles Prepared by Urea Homogenous Precipitation. *J. Clust. Sci.* **2015**, *26* (5), 1671–1681.

(30) Gu, J.; Ding, Y.; Ke, J.; Zhang, Y.; Yan, C. Controllable Synthesis of Monodispersed Middle and Heavy Rare Earth Oxysulfide Nanoplates Based on the Principles of HSAB Theory. *Acta Chim. Sin.* **2013**, *71* (3), 360.

(31) Pasberg, N.; den Engelsen, D.; Fern, G. R.; Harris, P. G.; Ireland, T. G.; Silver, J. Structure and Luminescence Analyses of Simultaneously Synthesised (Lu 1?x Gd X) 2 O 2 S:Tb 3+ and (Lu 1?x Gd X) 2 O 3 :Tb 3+. *Dalt. Trans.* **2017**, No. 4.

(32) Flahaut, J.; Guittard, M.; Patrie, M. Les Oxysulfures Me2O2S Des Éléments Du Groupe Des Terres Rares. *Bull. Soc. Chim. Fr.* **1958**, *7*, 990–994.

(33) Sourisseau, C.; Cavagnat, R.; Mauricot, R.; Boucher, F.; Evain, M. Structure and Bondings in Cerium Oxysulfide Compounds I - Electronic, Infrared and Resonance Raman Spectra of Ce2.0O2.5S. *J. Raman Spectrosc.* **1997**, *28* (12), 965–971.

(34) Sourisseau, C.; Fouassier, M.; Mauricot, R.; Boucher, F.; Evain, M. Structure and Bonding in Cerium Oxysulfide Compounds. II—Comparative Lattice Dynamics Calculations on Ce2O2S and Ce2.0O2.5S. *J. Raman Spectrosc.* **1997**, *28* (12), 973–978.

(35) Dugué, J.; Carré, D.; Guittard, M. Etude Structurale Des Oxysulfures de Cérium(III) et Cérium(IV). I. Structure Cristalline de l'Oxysulfure de Cérium Ce4O4S3. *Acta Crystallogr.* **1978**, *B34*, 3564–3568.

(36) Dugué, J.; Carré, D.; Guittard, M. Etude Structurale Des Oxysulfures de Cérium(III) et Cérium(IV). II. Structure Cristalline de l'Oxysulfure de Cérium Ce6O6S4. *Acta*

Crystallogr. **1979**, *B35*, 1550–1554.

(37) Cheng, J.; Zhu, J.; Wei, X.; Shen, P. K. Ce 2 O 2 S Anchored on Graphitized Carbon with Tunable Architectures as a New Promising Anode for Li-Ion Batteries. *J. Mater. Chem. A* **2015**, *3* (18), 10026–10030.

(38) Yang, L.; Cai, Z.; Hao, L.; Xing, Z.; Dai, Y.; Xu, X.; Pan, S.; Duan, Y.; Zou, J. Nano Ce 2 O 2 S with Highly Enriched Oxygen-Deficient Ce 3+ Sites Supported by N and S Dual-Doped Carbon as an Active Oxygen-Supply Catalyst for the Oxygen Reduction Reaction. *ACS Appl. Mater. Interfaces* **2017**, *9* (27), 22518–22529.

(39) Frank, P.; Hedman, B.; Carlson, R. M. K.; Tyson, T. A.; Roe, A. L.; Hodgson, K. A Large Reservoir of Sulfate and Sulfonate Resides within Plasma Cells from. *Biochemistry* **1987**, *26*, 4975–4979.

(40) Vairavamurthy, A.; Manowitz, B.; Luther, G. W.; Jeon, Y. Oxidation State of Sulfur in Thiosulfate and Implications for Anaerobic Energy Metabolism. *Geochim. Cosmochim. Acta* **1993**, *57* (7), 1619–1623.

(41) Prietzel, J.; Thieme, J.; Tyufekchieva, N.; Paterson, D.; Mcnulty, I.; Kögel-knabner, I. Sulfur Speciation in Well-Aerated and Wetland Soils in a Forested Catchment Assessed by Sulfur K -Edge X-Ray Absorption near-Edge Spectroscopy (XANES). *J. Plant Nutr. Soil Sci.* **2009**, *172*, 393–409.

(42) Morgan, B.; Burton, E. D.; Rate, A. W. Iron Monosulfide Enrichment and the Presence of Organosulfur in Eutrophic Estuarine Sediments. *Chem. Geol.* **2012**, *296–297*, 119–130.

(43) Rodriguez, J. A.; Chaturvedi, S.; Hanson, J. C.; Brito, J. L. Reaction of H2 and H2S with CoMoO4 and NiMoO4: TPR, XANES, Time-Resolved XRD, and Molecular-Orbital Studies. *J. Phys. Chem. B* **1999**, *103*, 770–781.

(44)   Rodriguez, J. A.; Jirsak, T.; Freitag, A.; Hanson, J. C.; Larese, J. Z.; Chaturvedi, S. Interaction of SO2 with CeO2 and Cu/CeO2 Catalysts: Photoemission, XANES and TPD Studies. *Catal. Letters* **1999**, *62* (2), 113–119.

(45)   Cui, D.; Zhang, P.; Ma, Y.; He, X.; Li, Y.; Zhang, J.; Zhao, Y.; Zhang, Z. Effect of Cerium Oxide Nanoparticles on Asparagus Lettuce Cultured in an Agar Medium. *Environ. Sci. Nano* **2014**, *1* (5), 459–465.

(46)   Gregson, M.; Lu, E.; Tuna, F.; McInnes, E. J. L.; Hennig, C.; Scheinost, A. C.; McMaster, J.; Lewis, W.; Blake, A. J.; Kerridge, A.; Liddle, S. T. Emergence of Comparable Covalency in Isostructural Cerium(<scp>iv</scp>)– and Uranium(<scp>iv</scp>)–carbon Multiple Bonds. *Chem. Sci.* **2016**, *7* (5), 3286–3297.

(47)   Ikeue, K.; Kawano, T.; Eto, M.; Zhang, D.; Machida, M. X-Ray Structural Study on the Different Redox Behavior of La and Pr Oxysulfates/oxysulfides. *J. Alloys Compd.* **2008**, *451* (1–2), 338–340.

(48)   Jiang, G.; Wei, X.; Zhou, S.; Chen, Y.; Duan, C.; Yin, M. Neodymium Doped Lanthanum Oxysulfide as Optical Temperature Sensors. *J. Lumin.* **2014**, *152*, 156–159.

(49)   Jiang, G.; Wei, X.; Chen, Y.; Duan, C.; Yin, M.; Yang, B.; Cao, W. Luminescent La2O2S:Eu3+ Nanoparticles as Non-Contact Optical Temperature Sensor in Physiological Temperature Range. *Mater. Lett.* **2015**, *143*, 98–100.

(50)   Bagheri, A.; Rezaee Ebrahim Saraee, K.; Shakur, H. R.; Zamani Zeinali, H. Synthesis and Characterization of Physical Properties of Gd2O2S:Pr3+ Semi-Nanoflower Phosphor. *Appl. Phys. A Mater. Sci. Process.* **2016**, *122* (5), 1–8.

(51)   Zhao, Q.; Zheng, Y.; Guo, N.; Jia, Y.; Qiao, H.; Lv, W.; You, H. 3D-Hierarchical Lu2O2S:Eu3+ Micro/nano-Structures: Controlled Synthesis and Luminescence Properties. *CrystEngComm* **2012**, *14* (20), 6659.

(52)   Wang, G.; Zou, H.; Zhang, B.; Sun, Y.; Huo, Q.; Xu, X.; Zhou, B. Preparation and Luminescent Properties of 1D Lu2O2S:Eu3+ Nanorods. *Opt. Mater. (Amst).* **2015**, *45*, 131–135.

(53)   Rosticher, C.; Viana, B.; Fortin, M.-A.; Lagueux, J.; Faucher, L.; Chanéac, C. Gadolinium Oxysulfide Nanoprobes with Both Persistent Luminescent and Magnetic Properties for Multimodal Imaging. *RSC Adv.* **2016**, *6* (60), 55472–55478.

(54)   Cichos, J.; Karbowiak, M.; Hreniak, D.; Stręk, W. Synthesis and Characterization of Monodisperse Eu3+ Doped Gadolinium Oxysulfide Nanocrystals. *J. Rare Earths* **2016**, *34* (8), 850–856.

(55)   Vegard, L. Die Konstitution Der Mischkristalle Und Die Raumfüllung Der Atome. *Zeitschrift für Phys.* **1921**, *5* (1), 17–26.

(56)   Denton, A. R.; Ashcroft, N. W. Vegard's Law. *Phys. Rev. A* **1991**, *43* (6), 3161–3164.

(57)   Uwamino, Y.; Ishizuka, T.; Yamatera, H. X-Ray Photoelectron Spectroscopy of Rare-Earth Compounds. *J. Electron Spectros. Relat. Phenomena* **1984**, *34* (1), 67–78.

(58)   Smart, R. S. C.; Skinner, W. M.; Gerson, A. R. XPS of Sulphide Mineral Surfaces: Metal-Deficient, Polysulphides, Defects and Elemental Sulphur. *Surf. Interface Anal.* **1999**, *28* (1), 101–105.

(59)   Manocha, A. S.; Park, R. L. Flotation Related ESCA Studies on PbS Surfaces. *Appl. Surf. Sci.* **1977**, *1* (1), 129–141.

Table of Content Graphic

Colloidal synthesis provides nanoparticles of (Gd,Ce)$_2$O$_2$S with controlled Gd:Ce ratio. Their crystal lattice parameter and their reactivity with air are strongly related to the cerium content. *In situ* X-ray spectroscopies reveal the nature of the surface as a function of cerium content.